EARTH SURFACE PROCESSES AND LANDFORMS
Earth Surf. Process. Landforms **37**, 1627–1640 (2012)

Published online 20 May 2012 in Wiley Online Library
(wileyonlinelibrary.com) DOI: 10.1002/esp.3263

Erosional power in the Swiss Alps: characterization of slope failure in the Illgraben

G. L. Bennett,[1]* P. Molnar,[1] H. Eisenbeiss[2] and B. W. McArdell[3]
[1] Institute of Environmental Engineering, ETH Zurich, Wolfgang-Paulistrasse 15, CH-8093, Switzerland
[2] Institute of Geodesy and Photogrammetry, ETH Zurich, Wolfgang-Paulistrasse 15, CH-8093, Switzerland
[3] Swiss Federal Research Institute WSL, Zürcherstrasse 111, CH-8903 Birmensdorf, Switzerland

Received 7 July 2011; Revised 28 March 2012; Accepted 11 April 2012

*Correspondence to: G. Bennett, Institute of Environmental Engineering, ETH Zurich, Wolfgang-Paulistrasse 15, CH-8093, Switzerland. E-mail: bennett@ifu.baug.ethz.ch

ESPL
Earth Surface Processes and Landforms

ABSTRACT: Landslides and rockfalls are key geomorphic processes in mountain basins. Their quantification and characterization are critical for understanding the processes of slope failure and their contributions to erosion and landscape evolution. We used digital photogrammetry to produce a multi-temporal record of erosion (1963–2005) of a rock slope at the head of the Illgraben, a very active catchment prone to debris flows in Switzerland. Slope failures affect 70% of the study slope and erode the slope at an average rate of 0.39 ± 0.03 m yr^{-1}.

The analysis of individual slope failures yielded an inventory of ~2500 failures ranging over 6 orders of magnitude in volume, despite the small slope area and short study period. The slope failures form a characteristic magnitude–frequency distribution with a rollover and a power-law tail between ~200 m^3 and 1.6×10^6 m^3 with an exponent of 1.65. Slope failure volume scales with area as a power law with an exponent of 1.1. Both values are low for studies of bedrock landslides and rockfall and result from the highly fractured and weathered state of the quartzitic bedrock.

Our data suggest that the magnitude–frequency distribution is the result of two separate slope failure processes. Type (1) failures are frequent, small slides and slumps within the weathered layer of highly fractured rock and loose sediment, and make up the rollover. Type (2) failures are less frequent and larger rockslides and rockfalls within the internal bedded and fractured slope along pre-determined potential failure surfaces, and make up the power-law tail.

Rockslides and rockfalls of high magnitude and relatively low frequency make up 99% of the total failure volume and are thus responsible for the high erosion rate. They are also significant in the context of landscape evolution as they occur on slopes above 45° and limit the relief of the slope. Copyright © 2012 John Wiley & Sons, Ltd.

KEYWORDS: landslides; rockfall; magnitude–frequency; power law; photogrammetry

Introduction

Slope failure is the main erosional process in many mountainous regions and may also be the most dangerous, making it important to quantify and characterize. Slope failure may be characterized statistically by its magnitude–frequency (MF) distribution, volume–area (VA) relation, and the slope gradient on which it occurs. The MF distribution of slope failure is an important tool for assessing slope failure hazard (Hantz *et al.*, 2003), detecting climatic and environmental change (Schlögel *et al.*, 2011) and in models of sediment transfer (Benda and Dunne, 1997; Fuller *et al.*, 2003) and is thus important to accurately define and understand. In the case that slope failure volumes are unknown, empirical relationships between slope failure area and volume may be used to convert areas into volumes (Malamud *et al.*, 2004) and associated erosion rates (Larsen *et al.*, 2010), making it important to constrain this relationship for different geological settings. Finally, quantifying the slope gradient at which slope failures of different magnitudes occur is important in hazard assessment (Guzzetti *et al.*, 1999) and in understanding landscape evolution (Densmore *et al.*, 1998; Korup *et al.*, 2010). However, the quantification and thus characterization of slope failure are restricted by the difficulty of obtaining accurate data, particularly volumetric data, from steep slopes that have often difficult access. In this study we used historical archives of aerial photographs to measure remotely the areas of past slope failures (Stark and Hovius, 2001; Brardinoni and Church, 2004; Stark and Guzzetti, 2009) and digital photogrammetry for measuring these in three dimensions (Schwab *et al.*, 2008) and computing volumes of slope failures and relevant erosion rates. Our study slope is at the head of a very active, steep mountain basin, prone to debris flows. Thus quantifying and characterizing slope failures are also important for understanding debris flow sediment transfer and hazard. We investigate the patterns and controls of channel sediment transfer in relation to hillslope sediment supply in a separate paper (Bennett *et al.*, submitted).

We use slope failure in this paper as a general term for the downslope movement of material that occurs when a slope becomes unstable. Categorization of slope failure is based on various characteristics such as the failure material (e.g. soil, debris, rock) and the mechanics of movement (e.g. slides,

slumps, falls, flows). Although the term 'landslide' encompasses a range of slope movements, such as soil slips, deep-seated slides, debris flows and rockfalls (Cruden and Varnes, 1996), studies of landslides reported in this paper generally focus on slope movements of the slide, slump and flow type in soil-mantled, vegetated and often forested slopes. Studies of rockfalls focus on this particular slope movement in rock slopes and cliffs. We make a further distinction in this study between slope failures following Katz and Aharonov (2006). Rockslides and rockfalls define failures that occur in a layered sequence or in pre-fractured solid rock, whereas earth/debris-slides and slumps occur in loose sediment and soils.

It has been observed that above a certain magnitude the frequency of landslides and rockfalls decays as a power-law (Hovius *et al.*, 1997; Hungr *et al.*, 1999; Stark and Hovius, 2001; Dussauge-Peisser *et al.*, 2002, 2003; Guzzetti *et al.*, 2002; Hergarten, 2002; Malamud *et al.*, 2004; Stark and Guzzetti, 2009; Lim *et al.*, 2010). Below this magnitude, the frequency often drops off, resulting in a transition within the probability density function (PDF) that is commonly referred to as the 'rollover'. Although the general shape of the MF distribution appears to be robust across different geologic and climatic settings (Malamud *et al.*, 2004), there is some variability in the power-law tails of the distribution. Possible causes of this variability include variability in material strength (Sugai *et al.*, 1994), climate (Li *et al.*, 2011), tectonics (Chen, 2009) and statistical noise (Korup *et al.*, 2012). Additionally, the origin of the characteristic MF distribution is debated. Some studies have suggested that the rollover present in many distributions is an artefact of undersampling of small failures (Stark and Hovius, 2001; Brardinoni and Church, 2004). Conversely, recent experimental and modeling studies suggest that it may have a physical origin (Katz and Aharonov, 2006; Stark and Guzzetti, 2009). These studies suggest that the characteristic landslide MF distribution is the combination of two separate slope failure processes: small failures of the slump and slide type within loose sediment and soil make up the rollover, and larger failures of the rockslide and rockfall type make up the power-law tail. This hypothesis is supported by the observation that the rollover is often absent from rockfall MF distributions (Malamud *et al.*, 2004). In order to be in a position to use MF distributions to detect climatic and environmental change and their effects on slope stability we need to better understand the controls on the shape of and variability in the MF distribution.

Several studies have found that landslide volume scales with area as a power law, $V \propto A^{\gamma}$, with an exponent γ (Simonett, 1967). Guzzetti *et al.* (2009) found γ=1.45 for 677 landslides worldwide, very close to the value of 1.5, leading them to conclude that the control on the relationship is geometrical and independent of physiographic setting. Many studies have used $\gamma = 1.5$ to convert areas into volumes and to estimate erosion rates (Hovius *et al.*, 2000; Lavé and Burbank, 2004; Malamud *et al.*, 2004; Gabet, 2007). However, Larsen *et al.* (2010) demonstrated significant variability in γ with hillslope material. They found lower γ values for soil landslides (1.1–1.3) than for bedrock landslides (1.3–1.6), which they attribute to the shallower failure depth of the former. The variability in γ is presumably the result of factors other than the soil/bedrock nature of the slope including error that is inherent to worldwide compilations that suffer from inconsistent measurement procedures. These points highlight the significance of empirically constraining γ for slopes with known geological characteristics.

In this study we aimed to (1) quantify slope failure from a mountain basin headwall over a 19 year period (1986–2005), (2) characterize the slope failures with regard to their MF, VA and depth–slope gradient relations, (3) explore variability in the characteristics of slope failures within the MF distribution, and (4) identify the relative importance of slope failures of different magnitudes in hillslope erosion and landscape evolution.

Study Site

The focus of this study is a 0.7 km^2 dominantly quartzitic rock slope within the northwest facing slopes of the Illhorn (2716 m a.s.l) at the head of the Illgraben catchment (Figures 1 and 2). Situated in the Rhone Valley in southwest Switzerland, this is an active, alpine, debris-flow catchment of high scientific interest due to a sediment discharge that exceeds Alpine standards by more than two orders of magnitude (Schlunegger *et al.*, 2009). Until now, the production of this sediment has been poorly quantified in comparison to the debris flow output.

The catchment has an area of 9.5 km^2, 4.6 km^2 of which is susceptible to debris flows (Figure 1). Debris-flow monitoring instruments were installed by the Swiss Federal Research Institute for Forest, Snow and Landscape (WSL) in 2000 and 2004 (Rickenmann *et al.*, 2001; Hürlimann *et al.*, 2003; McArdell *et al.*, 2007) to capture the magnitude and frequency of sediment output. Around 3–5 debris flows have been measured each year, which generally occur during intense summer thunderstorms (Badoux *et al.*, 2009) characteristic of the temperate-humid alpine climate. These make up an average annual sediment discharge of about 100,000 m^3.

The complex, highly fractured geology of the catchment (Figure 2) undoubtedly contributes to this high sediment output. The Illgraben trunk channel follows a thrust fault within the southwest striking axial plane of a large anticline, which forms the northern steep limb of the Penninic nappe stack. To the southeast and at the head of the channel the slopes are dominantly of quartzites and have been shown to contribute more than 50% of debris flow deposits (Schlunegger *et al.*, 2009). In the lower part of the catchment these quartzite slopes are heavily forested, while at the head of the channel, on the flanks of the Illhorn and including our study slope, the exposed slopes are up to 80° steep and are considered to be the dominant sediment source.

The study slope (Figure 2) covers an altitudinal range between 1250 m and 2370 m and spans a horizontal distance of 1250 m between the catchment crest and the head of the main debris-flow channel at its base. The perimeter was defined to be consistent with the sub-catchment scheme devised by Berger *et al.* (2011) using watershed analysis in ArcGIS. There are several contacts between different lithologies that cross cut the slope. The dominant geology is massive quartzite, which is intersected by bands of other quartzites (Figure 2). Dolomites crop out in the northwest part of the study slope as well as in thin bands towards the upper (southern) part of the slope where they are interbanded with schist and quartzite. The thrust fault, which the main debris flow channel follows, extends up, into and across the slope between the bands of quartzite. These are folded close to the surface and as a result are highly fractured. There is a discontinuous sediment cover on the slope from the rapid weathering of the underlying bedrock.

Several large historical slope failures are documented from the study slope and surrounding slopes. The most recent and best known of these is the rock avalanche of 26 March 1961 with an estimated volume of 3.5×10^6 m^3 (Gabus *et al.*, 2008). Other large events occurred in 1920, 1928 and 1934 (Gabus *et al.*, 2008). The deposits of an even older rock avalanche remain on the fan apex, thought to be of late Holocene age (Schürch, 2011). Berger *et al.* (2011) recorded 10 landslides of 300–4400 m^3 in volume that occurred between 2007 and 2009, the largest of which is 5 orders of magnitude smaller than the 1961 rock avalanche. These were a mixture of bedrock

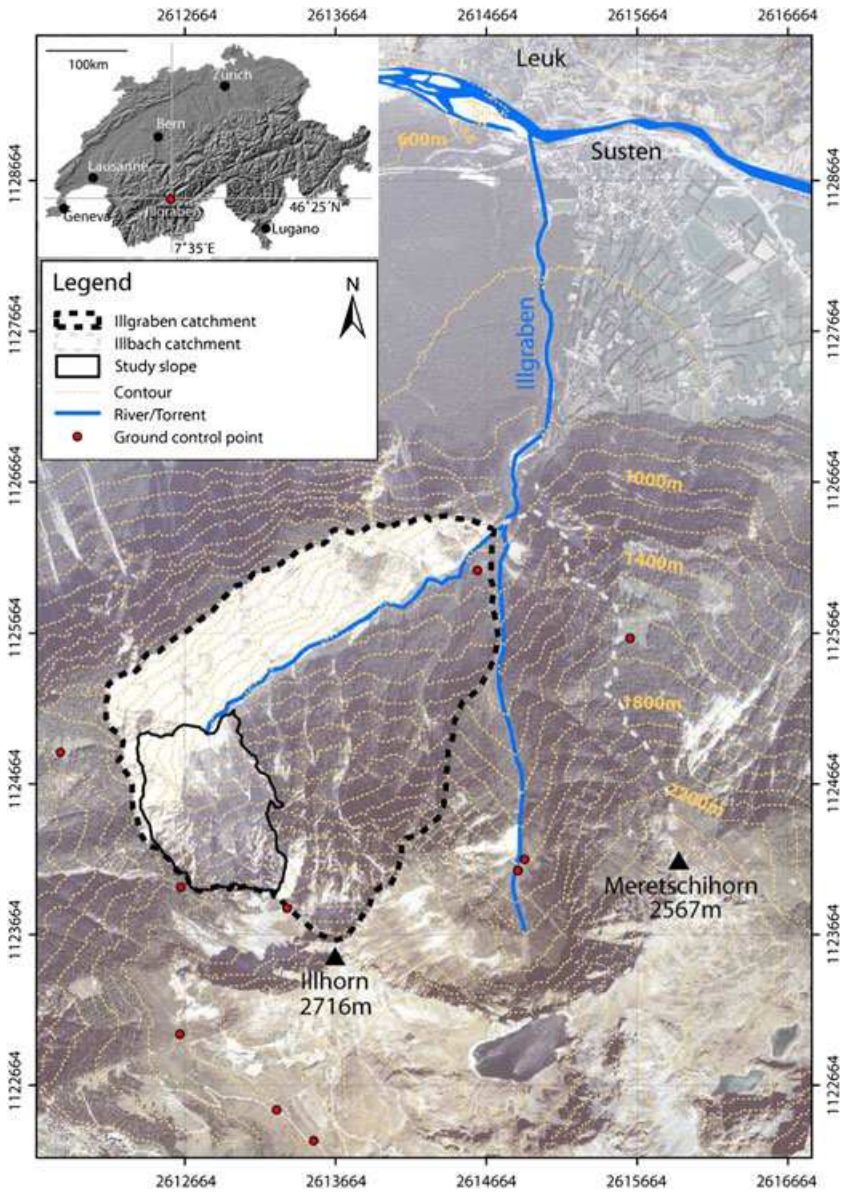

Figure 1. Location of the study slope in relation to the Illgraben catchment, the Rhône Valley and Switzerland. Ground control points used in the photogrammetric process are also shown. This figure is available in colour online at wileyonlinelibrary.com/journal/espl

slides and debris slides (termed 'alluvial landslides' in Berger *et al.*, 2011). Erosion rates of the slopes were estimated at up to 7 cm per year (Schlunegger *et al.*, 2009).

Methods

DEM preparation

Analogue aerial images of the Illgraben exist from around 1959 and have been flown repeatedly in time intervals of 1 to 17 years by the Swiss Federal Office of Topography (Swisstopo). Additionally, Swisstopo generated a DEM in 2005 for elevations below 2000 m using airborne Lidar. This has a resolution of 2 m and standard error of 0.5 m in altitude. We initially generated DEMs for 1963 and 1986 so as to produce two periods of analysis, 1963–1986 and 1986–2005 of comparable length. Following successful DEM generation from these aerial images and calculation of a particularly high erosion rate of $0.39 \pm 0.03\ \mathrm{m\,yr^{-1}}$ for the latter period, we generated two additional DEMs for 1992 and 1998, giving three additional 6/7 year periods of analysis: 1986–1992, 1992–1998 and 1998–2005 in which to measure slope failure in more detail.

The aerial images were first orientated in Leica Photogrammetry Suite 9.2 (LPS). An image stereo pair was set up for each year. This procedure involves the input of the parameters of the acquisition camera obtained from the camera calibration certificates (Table I), and the location of Ground Control Points (GCPs). GCPs used were those collected for the study by Berger *et al.* (2011). A minimum of six GCPs were located along with additional tie-points. LPS uses a one-step bundle adjustment for GCPs and tie points. This resulted in a global accuracy of between 0.37 and 0.47 pixels for the different stereo pairs (Table II).

The root mean square error (RMSE) of the GCPs in ground space ranges from 0.02 to 0.19 m in planimetry and height (Table II), indicating the precision of the GCP coordinates. The accuracy of the GCPs in image space resulted in less than half a pixel, indicating the acceptable quality of the image orientation.

DEM generation from the oriented aerial images was performed in ETH-developed SAT PP (Satellite image Precision Processing, ETH Zurich) following a similar procedure to Fischer *et al.* (2011). This software package has significant advantages over commercial packages, notably a more sophisticated image matching algorithm using a coarse-to-fine hierarchical solution that combines several image matching algorithms and automatic quality control (Zhang, 2005). For each set of images the exterior

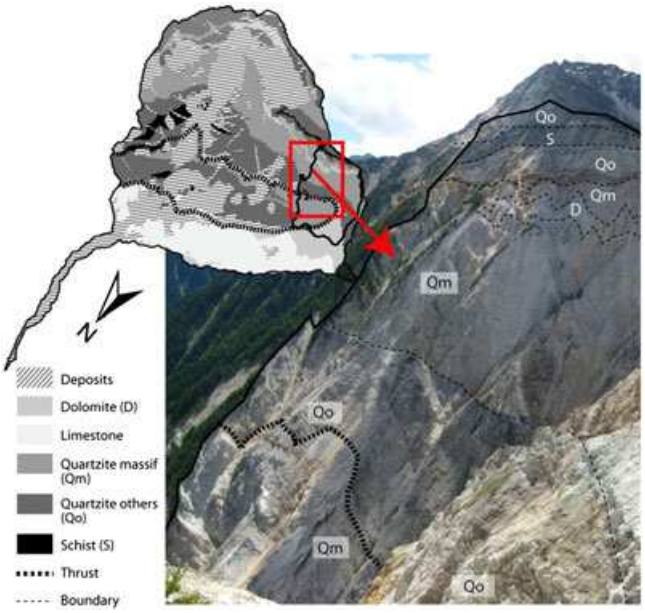

Figure 2. Geology of a part of the study slope in the Illgraben catchment (photograph) in relation to the geology of the Illgraben and Illbach catchments. Geological map adapted from Gabus *et al.* (2008). This figure is available in colour online at wileyonlinelibrary.com/journal/espl

orientation parameters obtained in LPS were imported and the images pre-processed, involving noise reduction, edge enhancement and production of image pyramids. The images were then matched based on least squares matching. In-depth descriptions of these procedures are given by Gruen *et al.* (2005); Zhang (2005) and Zhang and Gruen (2006). Seed points were measured manually to constrain automatic image matching. Typically 100 points were located for each set of images, with a broad coverage across the image space and with additional points on steep faces and along the channel. Finally, DEMs were extracted automatically with a resolution dictated by the resolution of the aerial images, which led to a grid size in Table I of 4 m for 1963 and 2 m for the remaining years.

We co-registered all the DEMs to the 2005 Swisstopo DEM so as to ensure a common reference, remove any systematic shift in the individual DEMs and to enable a direct comparison of the DEMs. Automatic co-registration of the DEMs on the reference DEM was performed in LS3D (Least Squares 3D Matching; Akca, 2010). Specifically, this was a local co-registration, meaning that the DEM was transformed onto the reference DEM based on a number of unchanged zones. Seven unchanged zones of at least 1000 m^2 were selected manually across the catchment within known stable terrain. This procedure utilizes the Generalized Gauss–Markoff model, minimizing the sum of squares of the Euclidean distances between the surfaces (Gruen and Akca, 2005). The transformation resulted in a standard deviation of registration error within these zones, which is an indication of the relative accuracy of the DEM compared with the reference DEM (Table III). The relative error of the DEMs compared with the reference DEM ranged between 2 and 2.7 m.

Uncertainty analysis

In the multi-temporal comparison of the DEMs the combined error in elevation change between two DEMs has a standard deviation, which was calculated as (Taylor, 1997):

$$\sigma_{diff} = \sqrt{\sigma_1^2 + \sigma_2^2} \tag{1}$$

with σ_1^2 and σ_2^2 being the standard deviations of registration errors of the individual DEMs. The standard error σ_{diff} ranges between 2.3 and 3.4 m (Table III). In the use of Equation (1) we assume that the uncertainties in the DEMs are independent (Lane *et al.*, 2003). Each elevation difference $\Delta z = z_1 - z_2$ between two DEMs can be converted to a t statistic:

$$t = \frac{z_1 - z_2}{\sigma_{diff}} = \frac{\Delta z}{\sigma_{diff}} \tag{2}$$

We consider the elevation change to be statistically significant if $|t| > 1$, representing 68% confidence that the elevation change is significant, which is the same level of confidence used by Brasington *et al.* (2000) and Lane *et al.* (2003). Therefore in the elevation change distributions (Figure 3(a), (b)), regions with elevation change smaller than σ_{diff} were considered uncertain and were not considered in the analysis of elevation change.

In calculations of volumetric change we extended the estimation of elevation change uncertainty to volume changes following Lane *et al.* (2003). The volume uncertainty σ_v for the case of spatially uniform σ_{diff} is:

$$\sigma_v = d^2.\sqrt{n}.\sigma_{diff} \tag{3}$$

where d is the cell size and n is the number of cells in each area of change. The measure of uncertainty σ_v was computed for individual landslides as well as for the entire areas of erosion and deposition.

Slope failure analysis

Analysis of erosion rates

To calculate erosion rates we (1) delineated areas of negative elevation change (erosion) above the σ_{diff} threshold of uncertainty in the elevation change maps; (2) calculated the volume of erosion using a grid-based calculation that takes the vertical distance between the corresponding cells in the DEMs; and finally (3) divided this volume by the area of the study slope and the period duration.

Extraction of areas and volumes of slope failures

We delineated slope failures from the areas of erosion in the elevation change maps (e.g. Figure 4(a), (b)) for periods B1–B3 using the raster to polygon tool in ArcGIS. In order to understand the sensitivity of the results to the procedure by which individual slope failures are extracted from the elevation change

Table I. Aerial photograph parameters.

Year	Date	Source	Photo numbers	Camera	Focal length (mm)	Average flight height (m)	Ground resolution (m)
1963	13.09.	Swisstopo	1094, 1095	Aviogon RC5	115.29	3047	0.63
1986	10.07.	Swisstopo	7759, 7758	Wild RC10	153.37	3712	0.34
1992	18.08.	Swisstopo	0834, 0835	Wild RC20	152.92	3104	0.38
1998	8.08.	WSL	7185, 7184	Wild RC30	153.51	3377	0.38

Table II. DEM and georeferencing parameters.

DEM	GCPs	Resolution (m)	Total image RMSE (pixel)	Control point RMSE (m) x,y,z	Control point RMSE (pixels) x,y
1963	7	4	0.466	0.19, 0.17, 0.11	0.48, 0.45
1986	6	2	0.369	0.04, 0.09, 0.04	0.31, 0.40
1992	6	2	0.394	0.07, 0.09, 0.02	0.30, 0.44
1998	6	2	0.384	0.06, 0.17, 0.05	0.29, 0.28

Table III. Results of registration and error analysis. σ_{reg} is the standard deviation of registration error. σ_{diff} is the standard deviation of the combined error in elevation between two DEMs.

Year	σ_{reg} (m)	Time period	σ_{diff} (m)
1963	2.72	1963–1986	3.4
1986	2.05	1986–1992	3.1
1992	2.29	1992–1998	3.2
1998	2.21	1998–2005	2.3

maps we used two methods. (1) We delineated all areas of negative elevation change (erosion) over the σ_{diff} threshold of error ($\Delta z > \sigma_{diff}$). In procedure (2) only areas of elevation change above 5 m were delineated ($\Delta z > 5$ m). This is a more conservative estimate of the error roughly corresponding to a 90% confidence bound and is constant between the periods. This higher threshold resulted in the division of some of the areas of erosion into more likely individual failures, although it removes a significant proportion of the eroded area. We calculated the volumes of the failures as described in point (2) of the section 'Analysis of erosion rates'.

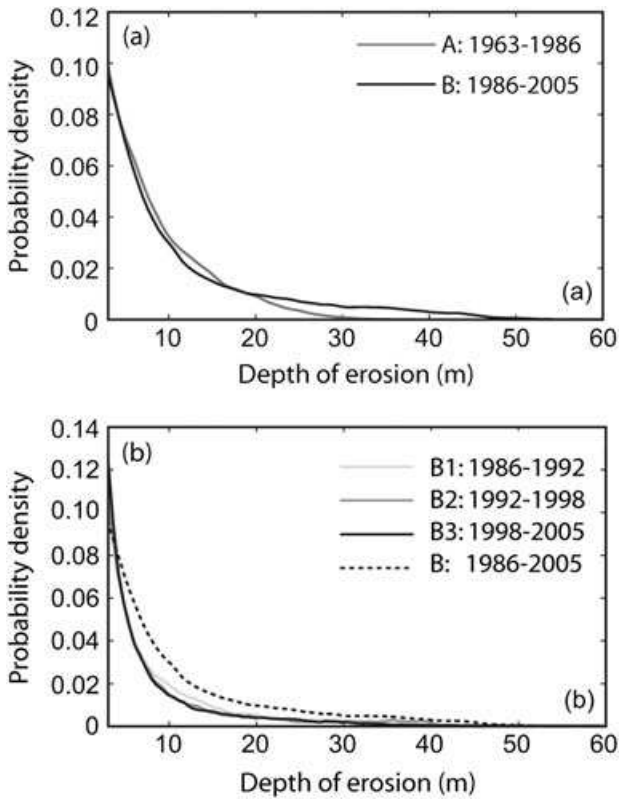

Figure 3. Probability distribution of erosion depth for: (a) periods A (1963–1986) and B (1986–2005); (b) sub-periods B1 (1986–1992), B2 (1992–1998) and B3 (1998–2005). Only statistically significant erosion of over 3 m, the mean σ_{diff}, is shown in each plot.

Magnitude–frequency analysis

There are two main ways in which to visualize and model slope failure MF with a power-law distribution in the tail. The first is to use the PDF:

$$p(x) = Cx^{-\beta} \tag{4}$$

where x is the quantity of interest (e.g. landslide area or volume), C is a normalization constant and β is the scaling exponent of the tail of the distribution ($\beta > 1$). This approach requires the binning of incremental magnitude values into bins of predefined width. Because the probability density diverges as $x \to 0$, there must be a lower bound, $x_{\min}$, to the power law behavior which is contained in the normalization constant, C.

The second is to use the complementary cumulative distribution function (CCDF), which is obtained by integrating Equation (4):

$$P(x) = \mathrm{P}(X \geq x) = \left(\frac{x}{x_{\min}}\right)^{-\rho} \tag{5}$$

where $P(x)$ is the probability of a randomly picked failure volume exceeding x and ρ is the slope of the CCDF and is related to β by:

$$\rho = \beta - 1 \tag{6}$$

The use of the CCDF is thought to be preferable to the PDF in estimation of the scaling exponent as it avoids the ambiguities introduced by arbitrary selection of bin sizes or scale (Brardinoni and Church, 2004; Hungr *et al.*, 2008). However, the rollover is more easily visualized in the PDF, making both useful in MF analysis.

We compiled a list of many studies that have reported MF distributions of both rockfalls and generic landslides using variations of the methods presented above (Table IV). This list omits many of the studies of landslides that are listed in a similar table in Van den Eeckhaut *et al.* (2007) but includes additional studies of rockfalls. Furthermore, we have cross-referenced estimates of β and ρ using equation (6) so as to aid comparison of these.

To make comparisons with many previously published landslide distributions, we plotted the empirical distributions of datasets (1) and (2) in PDF form in Figure 5(a). We extracted the frequency of different slope failure volumes using a kernel density estimate, which is considered to be a more robust measure of frequency variations than the traditional histogram (Silverman, 1981). We applied a kernel density estimate using a box kernel with a width of 0.4 to the log-transformed volume data. We experimented with different kernel widths and found a width of 0.4 to best capture the frequency variations in the data and we normalized the frequency by the bin width (Malamud *et al.*, 2004).

We estimated the β of the power-law tail, which contains ~99% of the failure volume by three methods: (1) robust linear regression between the logarithmically transformed frequency (f) and the equivalent logarithmically transformed volumes; (2) maximum likelihood estimation of β and estimation of $x_{\min}$ with fitting to the CCDF following Clauset *et al.* (2009) (Figure 6 (a), (b)); and (3) robust linear regression on the CCDF. Both methods (1) and (3) required definition of the minimum volume at which power-law scaling of slope failure frequency starts ($x_{\min}$) and below which data were excluded from linear

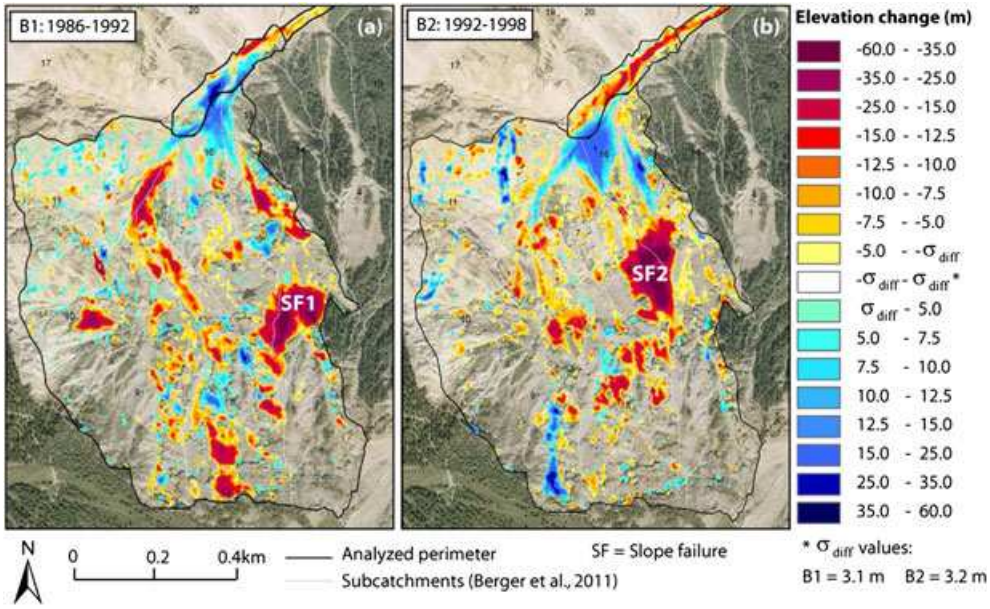

Figure 4. Spatial distribution of elevation change, including deposition, in the study slope and at the channel head for: (a) sub-period B1 (1986–1992); (b) sub-period B2 (1992–1998), and location of the largest slope failures (SF1 and SF2). This figure is available in colour online at wileyonlinelibrary.com/journal/espl

regression. This threshold was estimated from method (2), which allows an objective estimation of x_{min}, β and the likelihood p that the tail is power-law distributed.

While the PDF was useful to visualize the MF distribution, particularly the rollover, we find that the power law exponent estimated by linear regression from the PDF is biased and not recommendable. Other estimation methods such as the MLE or Hill's estimator are advisable (Hill, 1975; Clauset *et al.*, 2009). A particular benefit of the procedure proposed by Clauset *et al.* (2009) is the estimation of the minimum magnitude for power law scaling and the fit to the power law tail (p-value), which are difficult to obtain from previous studies that have used PDF or indeed other methods of fitting to the CCDF.

Volume–area and depth–gradient relations

To fit the empirical VA relationship to the data, the data were logarithmically transformed and fit using robust linear regression (Figure 7). The logarithmic transformation overcomes problems with fitting of data spanning multiple orders of magnitude. Guzzetti *et al.* (2009) showed that γ is not very sensitive to the exact fitting technique but suggested that robust linear regression is preferable as this reduces the effect of outliers.

Lastly, we explored where slope failures are likely to occur in space by looking at the relationship between mean failure depth and mean slope gradient of the pre-failure surface for failures of $V < x_{min}$ and $V \geq x_{min}$ (Figure 8).

Results

Erosion rates

The mean erosion rate increased from $0.24 \pm 0.003\,m\,yr^{-1}$ in 1963–1986 (period A) to $0.39 \pm 0.03\,m\,yr^{-1}$ in 1986–2005 (period B). Figure 3(a) shows that this increase in erosion rate is due to an increase in the mean depth of erosion from 7.5 m to 9.1 m and maximum depth of erosion from 38.7 m to 60 m in the two periods. Figure 3b shows the distribution of erosion depths in the three shorter periods of analysis (B1–B3) within B. There is a higher probability of shallower erosion for each sub-period B1 –B3 compared with the entire period B due to the coalescence of slope failures and thus an increasing depth of erosion through time.

Magnitude–frequency distributions

Delineation of slope failures described earlier produced two inventories. Procedure (1) produced an inventory of 2170 slope failures that affected 70% of the total slope area (dataset (1)). Procedure (2) produced a smaller inventory of 1475 slope failures that affected 48% of the slope area (dataset (2)). Both inventories span six orders of magnitude in area and seven orders of magnitude in volume.

The empirical MF distributions of datasets (1) and (2) (Figure 5 (a)) have a characteristic form with rollover and power-law tail. The rollover is located at the modal failure volume (rollover magnitude) of ~50 m^3. We plotted the volumetric uncertainty around dataset (1). This uncertainty results in some uncertainty in the rollover magnitude ($\pm \sim 20\,m^3$) but not in the form of the power-law tail.

Values of β we obtained using MLE and linear regression on the CCDF are consistently around 1 (or more) higher than those obtained by linear regression to the PDF (Table V). This bias is real and has been shown numerically (Clauset *et al.*, 2009). In fact, β estimated from the PDF for datasets (1) and (2) is less than 1, which is not feasible. The p −values of the power-law models estimated from the CCDF using MLE are all close to 1 and much higher than 0.1, meaning that the power law model gives a good fit to the data (Clauset *et al.*, 2009). All our estimated values of β and x_{min} for datasets (1) and (2) fall in between values reported for rockfall and landslides (Table IV).

Although the empirical probability distributions of slope failures within period B (Figure 5(b)) all show heavy tails, there is some variability in the power law exponents. The problem of binning is particularly evident in this plot with many of the larger values contained within the same frequency bin. Table VI gives the estimates of the power law exponent for the different periods, which may indicate sampling variability or different slope failure triggering histories in the periods.

Several studies that have investigated the causes of temporal variability in the MF distribution for a particular slope have attributed this to externally induced changes in slope stability

Table IV. Comparison of values of the exponents of the power law tails (***β*** and***ρ***) obtained for landslide and rockfall inventories, including this study, ordered from low to high β. R = Rockfall, L = Landslide, V = Volume, A = Area. H = Historical, E = Event-based. Values in bold are those reported in the studies.

Study	Slope failure type	Geological setting	Historical or event based	Time window	Attribute*	Range of power law fit**	slope of PDF (β)	slope of CDF (ρ = β-1)
Malamud *et al.*, 2004	R	Mixed	H	Mixed	V	10^{-3}-10^{6} m³ (9)	**1.07**	0.07
Guzzetti *et al.*, 2003	R	Granitic cliffs	H	145 years	V	10^{-1}-10^{6} m³ (7)	**1.1**	0.1
Dussauge-Peisser *et al.*, 2002	R	Calcareous cliffs	H	60 years	V	10^{1}-10^{6} m³ (5)	1.41	**0.41 ± 0.11**
Hungr *et al.*, 1999	R	Massive felsic rock	H	30 years	V	10^{-2}-10^{4} m³ (6)	1.43	**0.43**
Dussauge-Peisser *et al.*, 2002	R	Metamorphic and sedimentary rocks	H	22 years	V	10^{1}-10^{3} m³ (2)	1.45	**0.45 ± 0.15**
Dussauge-Peisser *et al.*, 2002	R	Granitic cliffs	H	78 years	V	50-10^{6} m³ (6)	1.46	**0.46 ± 0.11**
Dussauge-Peisser *et al.*, 2003	R	Undifferentiated rock cliffs	H	10000 years	V	10^{2}–10^{10} m³ (8)	1.52	**0.52**
Hungr *et al.*, 1999	R	Jointed metamorphic rock	H	22 years	V	10^{-1}-10^{4} m³ (5)	1.65	**0.65**
This study (Dataset (1))	L/R	Quartzitic rock and sediment	H	19 years	V	10^{2} -10^{6} m³ (4)	**1.65**	0.65
Gardner, 1970	R	Calcareous and quartzitic rock	H	2 summer periods	V	10^{-2}-10 m³ (5)	1.72	**0.72**
This study (Dataset (2))	L/R	Quartzitic rock and sediment	H	19 years	V	10^{3} -10^{6} m³ (3)	**1.76**	0.76
Lim *et al.*, 2010	R	Sandstone + mudstone capped in glacial till	H	20 months	V	10^{-6} - 10^{3}m³ (7)	1.8	**0.8**
Malamud *et al.*, 2004	L	Various	E	mixed	V (from A)	10^{6}-10^{6} m² (2)	**1.93**	0.93
Stark and Guzzetti, 2009	L	Sandstones, marls, limestones	H	17 years and 28 years	V (from A)	10^{3} - 10^{5} m² (2)	2	**1**
Rousseau, 1999	R	Basaltic cliff	H	2 months	V	1.5 orders magnitude	2	**1**
Stark and Hovius, 2001	L	Vegetated slopes with thin regolith cover	H	2 years	A (eroded)	10^{3}-10^{6} m² (3)	2.11	**1.11**
Stark and Guzzetti, 2009	L	Clay and silt and clastic sediments.	H	17 / 28 years	A (disturbed)	10^{3} - 10^{5} m² (2)	2.19	**1.19**
Malamud *et al.*, 2004	L	Weakly cemented clastic sediment	E	few hours	A (disturbed)	10^{3}-10^{5} m² (2)	**2.4**	1.4
Malamud *et al.*, 2004	L	Clay and silt and clastic sediments.	E	weeks	A (disturbed)	10^{3}-10^{5} m² (2)	**2.4**	1.4
Malamud *et al.*, 2004	L	Soil, siltstone, volcanic rocks, phyllite and schist	E	2 months	A (disturbed)	10^{3}-10^{5} m² (2)	**2.4**	1.4
Stark and Hovius, 2001	L	Schists and gneisses with thin regolith cover	H	8 years	A (eroded)	~10^{3}-10^{6} m² (3)	2.48	**1.48**

*Eroded area is that of the failure scar; disturbed area includes the scar and the runout area; V (from A) are volumes calculated based on the empirical scaling relationship between area and volume, see text.
**Numbers in brackets are the orders of magnitude in the range of reported data.

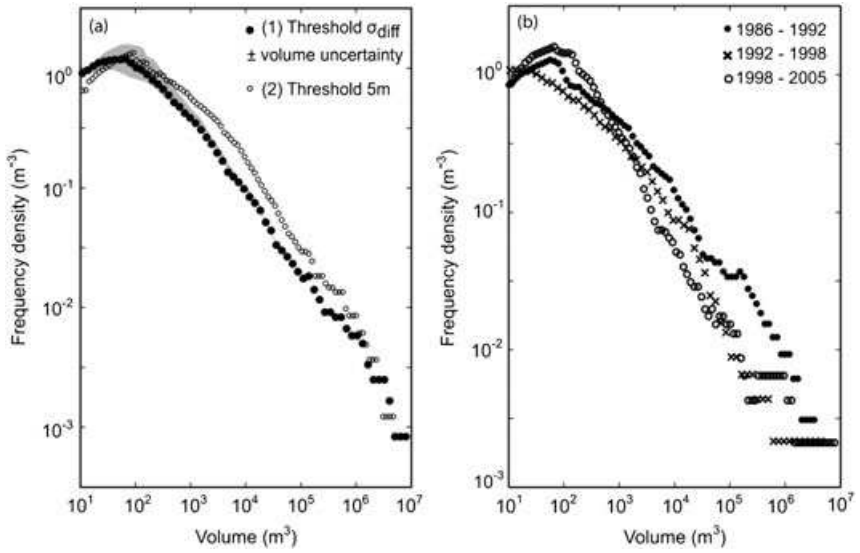

Figure 5. (a) Empirical frequency–volume distribution for logarithmically transformed datasets (1) and (2). Uncertainty in the volume of individual landslides is shown for dataset (1) as the grey range. The uncertainty is similar for dataset (2). (b) Distributions for temporal sub-periods B1–B3 within dataset (1).

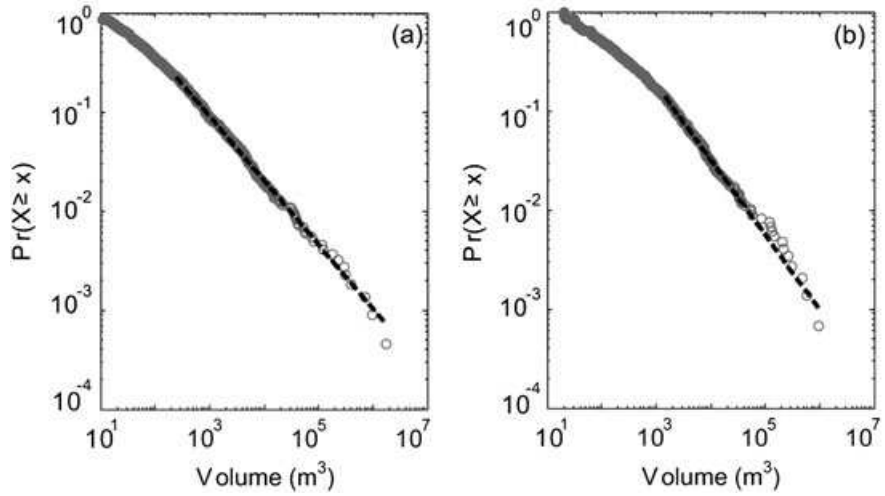

Figure 6. Complementary cumulative empirical distributions for (a) dataset (1) and (b) dataset (2), fit with theoretical power law model by the maximum likelihood method.

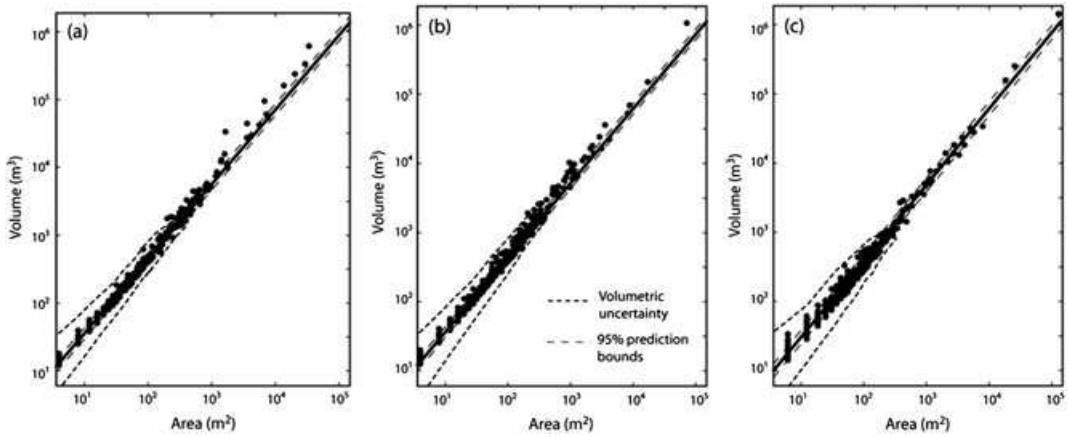

Figure 7. Volume–area distribution of log transformed dataset (1) split into the three periods of analysis: (a) B1: 1986–1992, (b) B2: 1992–1998, (c) B3: 1998–2005. Uncertainty in volumes is shown by the small dashed lines. Power-law fits are shown along with 95% prediction bounds. For model exponents see Table VII.

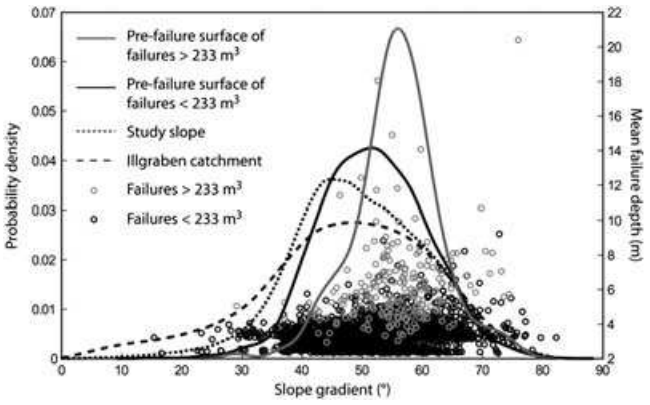

Figure 8. Relationship between mean failure depth and slope gradient of the pre-failure surface for failures > 233 m³ (grey circles) and failures < 233 m³ (black circles) on the right-hand axes along with their probability distributions (grey and black lines respectively), plotted against the probability distributions of slope gradient of the study slope and Illgraben catchment (Figure 1).

Table V. Comparison of frequency-volume relationship using the methods of least squares fitting (LS) to the PDF and CCDF and maximum likelihood estimation (MLE) based on the method of Clauset *et al.* (2009). p −values over 0.1 indicate a good fit to the power law distribution. 'Tail' refers to the power law tail, i.e. where $x \geq x_{min}$.

Attribute	Dataset (1)	Dataset (2)
LS (PDF) (β)	0.65	0.72
LS (CCDF) (β)	1.64	1.75
MLE (β)	1.65	1.76
p −value	0.76	0.93
x_{min}(m³)	233	1440
Equivalent A (m²)*	61	204
Number of failures (n)	497	205
Proportion of events in tail (%)	22.9	13.9
Volume of events in tail (m³)	6.25×10^6	5.07×10^6
% of total volume	98.7	96.1

*Calculated based on $\gamma = 1.1$ in Equation (7) and reported in Table VII.

(Chen, 2009; Li *et al.*, 2011; Schlögel *et al.*, 2011). However, a recent study by Korup *et al.* (2012) suggests that this variability may arise from statistical noise and that MF distributions may be powerless to detect environmental variability. It was beyond the scope of this paper to investigate the causes of temporal variability in the MF distribution. These are investigated in an additional study of the climatic and seismic controls on hillslope erosion and channel sediment transfer in the Illgraben (Bennett *et al.*, submitted).

Table VII. Comparison of volume–area relationship for projected and plan area and different periods using dataset (1). A is the projected area and A^* is the real surface area of the slope failure.

Area type	Attribute	Dataset (1)	B1: 1986–1992	B2: 1992–1998	B3: 1998–2005
A	α	0.41	0.46	0.48	0.32
	γ	1.1 ± 0.1	1.10	1.08	1.10
A^*	α	0.20	0.21	0.25	0.17
	γ	1.13 ± 0.1	1.09	1.07	1.06

Volume–area relation

We fitted the relationship between landslide volume and area of the form $V = \alpha A^{\gamma}$ to the data (Figure 7). For dataset (1) we obtained estimates of α=0.41 and γ=1.1 (Table VII). The exponent γ is similar for dataset (2) indicating that it is insensitive to the extraction procedure. We thus performed further sensitivity analyses of γ only on dataset (1).

Significantly, the exponent γ is practically constant between the different periods within dataset (1) (Table VII), showing that this relation is quite general for this geological setting. We also tested the sensitivity of the exponent to using real surface areas A^*, rather than projected areas A. Most studies report A (Malamud *et al.*, 2004). However, on steep slopes such as those in our basin A may be significantly smaller than the actual surface area A^*. We calculated the mean gradient θ for each slope failure based on the surface prior to the failure and multiplied A by $1/\cos(\theta)$. For the steepest slope A^* was more than 7 times A but this does not affect the estimate of γ significantly, only the intercept α (Table VII). However, volumetric uncertainty does propagate into uncertainty in γ. We estimated a range of exponents for the range of possible volumes of 1.02–1.31 for dataset (1).

The VA relation is dominated by the smallest failures ($< x_{min}$) as these make up ~80% of the total number of failures in our inventory (Table V). These have a small range of depths (Figure 8) such that larger failures are relatively thinner and thus smaller in volume relative to their area than small failures.

Pre-failure slope gradient of failures

The statistical distribution of slope failure volumes allows us to investigate detailed characteristics of the failures, such as mean

Table VI. Comparison of frequency–volume relationship using different methods for different periods within dataset (1) (B1–B3). p −values over 0.1 indicate a good fit to the power law distribution. The p −value is not reported for B2 as the number of landslides is too small for an accurate estimation of β. 'Tail' refers to the power law tail, i.e. where $x \geq x_{min}$.

Attribute	B1: 1986–1992	B2: 1992–1998	B3: 1998–2005
LS (PDF) (β)	0.56	0.71	0.63
LS (CCDF) (β)	1.59	2.04	1.68
MLE (β)	1.54	1.99	1.72
p − value	0.1		0.1
x_{min} (m³)	131	3975	59
Equivalent A (m²)*	32	773	21
Number of failures (n)	220	32	424
Proportion of events in tail (%)	37	4	53
Volume of events in tail (m³)	2.28×10^6	1.38×10^6	2.52×10^6
% of total volume	99	91	99

*Calculated based on values of $\boldsymbol{\alpha}$ and $\boldsymbol{\gamma}$ reported in Table VII for area type A.

failure depth as a function of pre-failure slope gradient in Figure 8. We found that failures of $V < x_{min}$ (233 m^3, Table V) have a small range of mean depths (~2–6 m) but a wide range of pre-failure slope gradients (~15–80°) and a mean gradient of ~50°. Failures of $V \geq x_{min}$ have a larger range of mean depths (~3–20 m) but narrower range of slope gradients and steeper mean gradient (~55°). The majority of failures of $V \geq x_{min}$ occur on slopes above 45° in slope gradient.

Discussion

Discussion of methodology

The main limitation of our analysis is the possibility that some of the slope failures in our inventory contain several individual failures that have coalesced over the 6–7 year time windows. While coalescence is inherent to any historical inventory of slope failures (e.g. many in Table IV) it is particularly true for our inventory given the high erosion rate. In order to assess the possible degree of coalescence of slope failures within these periods we looked at repeated failures between periods B1, B2 and B3. For failed cells in any one period we calculated the likelihood that there was failure in the equivalent cell in one or both of the other periods. This analysis suggests that at most 28% of slope failures are affected by coalescence. The manual delineation of individual landslide scars within a failed area from inspection of the photo pairs was, however, not possible due to the lack of any sort of vegetation cover, and so any pattern of post-landslide vegetation re-growth, and the subtle contrast between the substrate and freshly eroded debris.

While we cannot solve the problem of coalescence in our dataset, several points lead us to believe that the MF model is reliable. For instance (1) we modelled the sum of the failures in the different periods, so mimicking the coalescence over a single period, and obtained a similar exponent β=1.6; (2) we repeatedly drew two samples from our power-law model and modelled their sums and consistently obtained the same exponent, although slightly larger x_{min}; and finally, (3) we modelled the landslides measured in the study slope by Berger *et al.* (2011) on a seasonal basis between 2007 and 2009 where coalescence was not an issue, and observe that these also follow a power-law distribution with an exponent β=1.89 and x_{min}=300 m^3. Further confirmation of our MF model could be achieved by a higher temporal resolution study of slope failures over a period of multiple years.

The use of photogrammetry to produce high resolution (2 m) DEMs enabled us to capture small events within the MF distribution, which are sometimes undersampled, particularly in heavily forested terrain (Stark and Hovius, 2001; Brardinoni and Church, 2004). This may explain why we obtain a relatively small modal failure magnitude (peak of the rollover) of ~50 m^3 and a small failure magnitude for the start of power law scaling at x_{min}= ~ 200 m^3 in comparison with other studies of landslides (Table IV). This is an upper estimate of the rollover magnitude as coalescence may have decreased the frequency of the smallest events, but despite some uncertainty in its magnitude we suggest that the rollover does have a physical explanation, as we discuss in the following section.

A number of landslide studies have focused on modeling the whole MF distribution including the rollover (Stark and Hovius, 2001; Malamud *et al.*, 2004). Malamud *et al.* (2004) fit several landslide inventories with a three-parameter inverse Gamma distribution. Stark and Hovius (2001) fit their probability densities of landslides with a double Pareto distribution. Both of these distributions capture the rollover that characterizes landslide distributions for small landslides and the power-law tail for medium and large landslides. Stark and Hovius (2001) justify their effort to model their entire distribution of landslides in Taiwan by the observation that only 25% of their data are in the tail of their distribution. In our datasets, even less of the data are in the tail, 5–22%, but these make up between 96 and 99% of the total failed volume (Table V). This indicates the importance of this part of the distribution to the overall sediment budget at the Illgraben. We therefore focused on modeling this part of the distribution, rather than attempting to describe the entire distribution with more complex models. Such models are more appropriate for rockfall hazard assessments, in cases that small slope failure volumes pose a significant hazard.

Physical interpretation of our dataset

A distinction between the MF distribution of generic landslides and rockfalls is apparent in Table IV. Exponents β reported for landslides between 1.93 (Malamud *et al.*, 2004) and 2.44 (Stark and Hovius, 2001) are consistently higher than those for rockfall of between 1.07 (Malamud *et al.*, 2004, based on various datasets) and 2 (Rousseau, 1999). The power-law exponent in the MF relation that we obtained for dataset (1), β=1.65, is at the upper end of values found for rockfall and lower end of values found for landslides. All the studies reported in Table IV that have obtained smaller exponents have investigated rock slopes of stronger bedrock (mainly granites and metamorphic rocks). Conversely, all studies that have obtained larger exponents have investigated rock slopes either of weaker bedrock (Lim *et al.*, 2010) or soil-mantled slopes in which deep and large failures are less common. Our exponent is similar to that obtained by Gardner (1970) who also studied failures in quartzitic rock slopes. Our study supports the hypothesis that the value of β increases, and thus that large events are less frequent, when slope strength, as determined by cohesion (C) and friction angle (ϕ), decreases (Dussauge-Peisser *et al.*, 2002). This is also in accordance with the erosion model proposed by Densmore *et al.* (1998).

The VA relationship has been widely used to convert areas of landslides into volumes and to calculate erosion rates from these (Table IV). The accurate calculation of γ is thus pertinent to the calculation of erosion by landslides. Larsen *et al.* (2010) suggested that γ could be used to differentiate between soil and bedrock landslides on the basis that the former have a lower range of γ (1.1–1.3) than the latter (1.3–1.6) in their global study of landslides. Our range of γ (1–1.3) is similar to that found for soil-based landslides rather than bedrock-landslides, despite the bedrock nature of our slope. The low γ –value results from the small depth of failures relative to their areas, which we hypothesize is due to the granular and incohesive nature of the highly fractured quartzite bedrock, which fails at relatively shallow depths for a rock slope. Our result demonstrates the difficulty of generalizing at this first-order level of complexity (soil or bedrock) and caution against the application of an exponent developed from one study area to another based simply on the nature of landsliding (soil or bedrock) (Larsen *et al.*, 2010). This is particularly pertinent concerning the calculation of erosion rates for the reason that the erroneous selection of γ may result in making large errors in the landslide volumes and erosion rates derived from these (Larsen *et al.*, 2010). More studies like this one are needed that constrain γ for different geological settings.

On the basis of our analysis and observations of the slope we hypothesize that erosion of the study slope occurs by two failure processes (Figure 8), based on the hypothesis of Katz and Aharonov (2006).

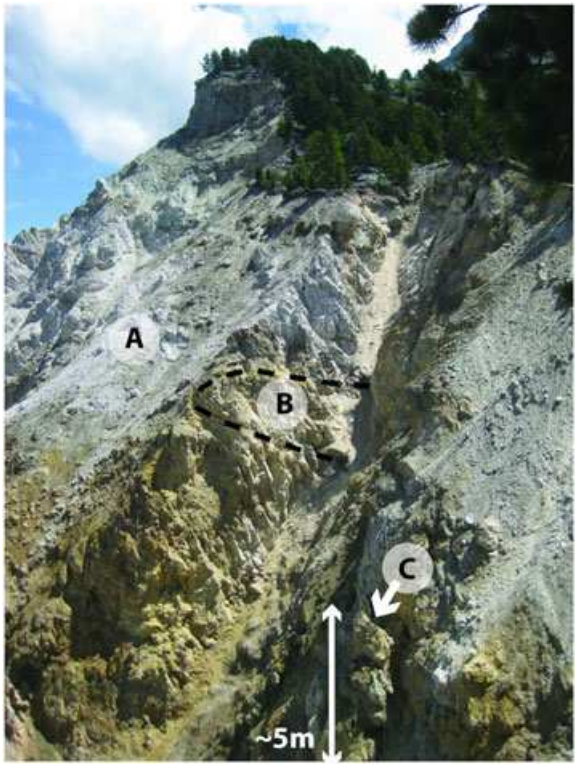

Figure 9. Example of the environment of type (1) failures: the upper 5 m of weathered rock and unconsolidated sediment. A = loose sediment cover; B = fold in the quartzites cropping out at the surface; C = imminent failure of ~5 m depth. This figure is available in colour online at wileyonlinelibrary.com/journal/espl

Type (1) failures are smaller failures with $V < x_{min}$ (rollover part of the MF distribution) with a narrow depth range and wide range of pre-failure slope gradients. We hypothesize that these are slumps and slides within loose sediment and highly fractured bedrock that make up a relatively homogenous top layer of the slope that is exposed to physical and chemical weathering. Figure 9 is an example of the environment of failure. It shows a fold at the surface, around which the rocks are heavily fractured and disintegrated, and a discontinuous cover of loose sediment. The depth of the failures is determined by sediment availability on the slopes or the depth of this weathered layer. This failure type corresponds with the small slumps and slides failures found to occur within the top 5 m of a slope by Katz and Aharonov (2006) in their experimental study. The fact that some of our failures are relatively deep (>5 m) suggests that the weathered layer is quite deep. This is plausible considering the highly fractured nature and permeability of the quartzites and thus susceptibility to chemical and physical weathering (Jaboyedoff *et al.*, 2004). The narrow depth range results in a characteristic, or modal, size of around 50 m^3 for type (1) failures, giving a physical explanation for the presence of the rollover in our distribution.

Type (2) failures are larger failures with $V \geq x_{min}$ (power-law tail of the MF distribution) with a wide depth range and narrow range of pre-failure slope gradients. We hypothesize that these are rockslides and rockfalls that occur within layered and fractured bedrock. These have a depth determined by the location of failure surfaces within the slope and are generated mostly on very steep slopes (>45°) due to the forces needed to overcome the friction angle of the rock mass. Several factors may act to create potential failure surfaces in the study slope. The first is the presence of discontinuities between different geological units, which may behave as sliding surfaces (Dussauge-Peisser *et al.*, 2003). One of the largest slope failures (SF1 in Figure 4 (a)) occurred on the boundary between two rock types. Another large slope failure (SF2 in Figure 4(b)) occurred just above the

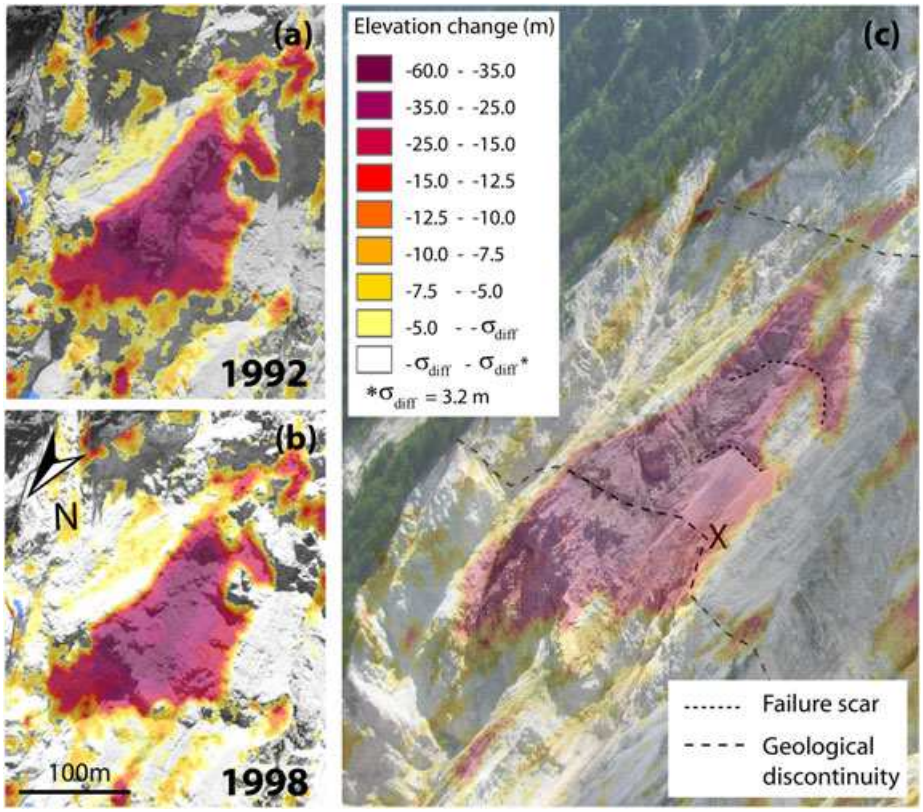

Figure 10. Example of a type (2) failure, SF2 in Figure 4(b). (a) 1992 orthophoto overlaid with the 1992–1998 elevation change map. (b) 1998 orthophoto overlaid with the same elevation change map. (c): Oblique photograph taken in July 2011 overlaid with the elevation change map. The relationship of SF2 to the thrust fault is clear. We observed water originating from this boundary at point X. This figure is available in colour online at wileyonlinelibrary.com/journal/espl

thrust fault that cross-cuts the bottom of the slope. A close up of SF2 is shown in Figure 10(a)–(c). The downslope locus of the failure occurred along the thrust fault and geological discontinuity (Figure 10c). We observed water originating from this boundary (X in Figure 10(c)). It is known that water along discontinuities enhances the fracturing process (Pelletier *et al.*, 1997). Another factor that may create potential failure surfaces is bedding plane strength variability (Pelletier *et al.*, 1997). In the massive quartzites we found layers of crushed quartzite crystals, which may reduce slope stability along potential failure surfaces. Jaboyedoff *et al.* (2004) describe how the existence of joints containing layers of crushed and weathered 'soil-like' material, known as fault gouge, played a fundamental role in the destabilization of the 1991 Randa rockslide, for example. These hypothesized mechanisms could be investigated by a geomechanical study of the slope along with a higher resolution study of slope failure in the rock face. Regardless of the exact mechanisms by which these failures occur, we suggest that it is the heterogeneous nature of the fractured and bedded rock that produces a wide range of failure depths and thus deviations from the characteristic landslide size and the emergence of a power-law distribution for type (2) failures (Katz and Aharonov, 2006).

The combination of both failure types gives the characteristic MF distribution with rollover and power-law tail. This study therefore lends some empirical support to the hypothesis of Katz and Aharonov (2006) that the complex MF distribution of landslides is the combined effect of these two processes.

The distribution of type (1) and type (2) failures with slope gradient is significant in understanding the evolution of rock slopes. The fact that type (1) failures have a slope gradient distribution almost identical to the study area suggests that the slopes in the area are generally very close to the local friction angle. 95% of the large type (2) failures occur at slopes above 45° in gradient, suggesting that this is a threshold above which these failures degrade the steep slopes and limit the local relief. This provides a physical basis for the use of the concept of a threshold hillslope angle for slope failure in many landscape evolution models (Densmore *et al.*, 1998).

Erosion rates of up to ~350 mm yr^{-1} (1986–2005) are much greater than previously reported rock slope erosion rates (Moore *et al.*, 2009). Averaged over the active part of the basin (4.6 km^2) this gives an annual erosion rate of about 61 mm. This is a lower estimate as it does not take into account erosion elsewhere in the catchment. This is an order of magnitude greater than the maximum erosion rates reported for glaciated basins and volcanic rivers (Koppes and Montgomery, 2009). We propose that a high density and favorable orientation of fractures and geological discontinuities result in low rock mass strength that predisposes the slope to failure. However, the rate of erosion is ultimately controlled by environmental factors that control the processes that act to degrade the slopes (Moore *et al.*, 2009) and which we investigate in an additional paper (Bennett *et al.*, submitted).

Conclusions

We used a digital photogrammetric processing procedure to produce a multi-temporal and high-resolution record of erosion of a steep rock slope at the head of the Illgraben catchment, Switzerland, spanning 42 years. The high erosion rate enabled us to extract a multi-temporal inventory of ~2500 slope failures that occurred in a period of particularly great erosion, 1986–2005. This was split in three sub-periods of 6/7 years. We characterized the slope failures based on their magnitude–frequency, volume–area and depth–slope gradient relations. We explored variability in the characteristics of slope failures in the magnitude–frequency distribution and identified the relative importance of slope failures of different magnitudes as contributors to erosion and landforming agents.

The slope failures have a characteristic magnitude–frequency distribution with a rollover at ~50 m^3 and a power-law tail between ~200 m^3 and 1.6×10^6 m^3 with a scaling exponent of 1.65. This exponent is at the upper end of values found for rockfalls within stronger bedrock and lower end of values found for landslides and rockfalls within weaker bedrock. This result supports the hypothesis that the value of the exponent increases, and thus that large events are less frequent, when slope strength, as determined by cohesion and friction angle, decreases.

The volume of the failures scales with area as a power law with a range of exponents γ = 1–1.3 resulting from volume uncertainty. These values are low for the bedrock nature of the slope, when comparing with a worldwide compilation of landslides. We hypothesize that this is due to the highly fractured and weathered state of the quartzitic bedrock, which fails at relatively shallow depths for bedrock.

Our analysis supports the hypothesis that the MF distribution is the result of two failure processes. Type (1) failures are frequent, small slides and slumps within an upper weathered layer of highly fractured rock and loose sediment. The depth of this layer limits the volume of the failures resulting in a modal failure volume, giving a physical explanation for the rollover. Type (2) failures are less frequent rockslides and falls within the internal bedded and fractured slope along pre-existing potential failure surfaces. The heterogeneous nature of the potential failure surfaces results in a wide range of failure depths, giving rise to the power law tail of the magnitude frequency distribution.

Rockslides and rockfalls of high magnitude and relatively low frequency are responsible for the high erosion rate of the study slope of 0.39 ± 0.03 m yr^{-1} as they make up ~99% of the total failure volume. They are also significant in the context of landscape evolution at the head of the catchment as they occur on slopes above 45° and limit the relief of the slope. This study therefore supports the concept of a threshold hillslope angle for slope failure in landscape evolution modeling.

Acknowledgements—This study was completed within the SedyMONT project, part of the ESF-funded TOPOEUROPE. Funding provided by the Swiss National Science Foundation Grant 20T021-120467 is acknowledged. Aerial photographs and 2005 Digital Elevation Model were provided by Swisstopo. Ground Control Points using in photogrammetric processing were provided by Catherine Berger. Many thanks to Rafael Caduff and James Glover for their geological insight and to Bettina Schaeppi for her help with the analysis.

References

Akca D. 2010. Co-registration of surfaces by 3D least squares matching. *Photogrammetric Engineering and Remote Sensing* **76**: 307–318.

Badoux A, Graf C, Rhyner J, Kuntner R, McArdell BW. 2009. A debris-flow alarm system for the Alpine Illgraben catchment: design and performance. *Natural Hazards* **49**: 517–539.

Benda L, Dunne T. 1997. Stochastic forcing of sediment supply to channel networks from landsliding and debris flow. *Water Resources Research* **33**: 2849–2863.

Bennett GL, Molnar P, McArdell BW, Schlunegger F, Burlando P. Submitted. Patterns and controls of sediment production and transfer in the Illgraben. *Geomorphology*

Berger C, McArdell BW, Schlunegger F. 2011. Sediment transfer patterns at the Illgraben catchment, Switzerland: Implications for the time scales of debris flow activities. *Geomorphology* **125**: 421–432.

Brardinoni F, Church M. 2004. Representing the landslide magnitude–frequency relation: Capilano River basin, British Columbia. *Earth Surface Processes and Landforms* **29**:115–124.

Brasington J, Rumsby BT, McVey RA. 2000. Monitoring and modeling morphological change in a braided gravel-bed river using high resolution GPS-based survey. *Earth Surface Processes and Landforms* **25**: 973–990.

Chen CY. 2009. Sedimentary impacts from landslides in the Tachia River basin, Taiwan, 2010–2099. *Geomorphology* **133**: 143–151.

Clauset A, Shalizi CR, Newman MEJ. 2009. Power-law distributions in empirical data. *SIAM Review* **51**: 661–703.

Cruden DM, Varnes DJ. 1996. Landslide types and processes. In *Landslides: Investigation and Mitigation*, Turner AK, Shuster RL (eds). Transportation Research Board, Special Report 247: 36–75.

Densmore AL, Ellis MA, Anderson RS. 1998. Landsliding and the evolution of normal-fault-bounded mountains. *Journal of Geophysical Research* **103**: 15203–15219.

Dussauge-Peisser C, Helmstetter A, Grasso J-R, Hantz D, Jeannin M, Giraud A. 2002. Probabilistic approach to rock fall hazard assessment: potential of historical data analysis. *Natural Hazards and Earth Systems Science* **2**: 15–26.

Dussauge-Peisser C, Grasso J-R, Helmstetter A. 2003. Statistical analysis of rock fall volume distributions: implications for rock fall dynamics. *Journal of Geophysical Research* **108**: 2286. DOI: 10.1029/2001JB000650.

Fischer L, Eisenbeiss H, Kääb A, Huggel C, Haeberli W. 2011. Monitoring topographic changes in a periglacial high-mountain face using high-resolution DTMs, Monte Rosa East Face, Italian Alps. *Permafrost and Periglacial Processes* **22**: 140–152.

Fuller CW, Willett SD, Hovius N, Slingerland R. 2003. Erosion rates for Taiwan mountain basins: new determinations from suspended sediment records and a stochastic model of their temporal variation. *Journal of Geology* **111**: 71–87.

Gabet EJ. 2007. A theoretical model coupling chemical weathering and physical erosion in landslide-dominated landscapes. *Earth and Planetary Science Letters* **264**: 259–265.

Gabus JH, Weidmann M, Bugnon P-C, Burri M, Sartori M, Marthaler M. 2008. Geological Map of Sierre 1:25 000 (LK 1278, sheet 111). In *Geological Atlas of Switzerland*. Swiss Geological Survey: Wabern, Switzerland.

Gardner J. 1970. Rockfall: a geomorphic process in high mountain terrain. *The Albertan Geographer* **6**: 15–20.

Gruen A, Akca D. 2005. Least squares 3D surface and curve matching. *ISPRS Journal of Photogrammetry and Remote Sensing* **31**: 151–174.

Gruen A, Zhang L, Eisenbeiss H. 2005. 3D precision processing of high-resolution satellite imagery. In Proceedings of the ASPRS 2005 Annual Conference, American Society for Photogrammetry and Remote Sensing, Behesda, Maryland.

Guzzetti F, Carrara A, Cardinali M, Reichenbach P. 1999. Landslide hazard evaluation: a review of current techniques and their application in a multi-scale study, Central Italy. *Geomorphology* **31**: 181–216.

Guzzetti F, Malamud BD, Turcote DL, Reichenbach P. 2002. Power-law correlations of landslide areas in Central Italy. *Earth and Planetary Science Letters* **195**: 169–183.

Guzzetti F, Ardizzone F, Cardinali M, Rossi M, Valigi D. 2009. Landslide volumes and landslide mobilization rates in Umbria, central Italy. *Earth and Planetary Science Letters* **279**: 222–229.

Guzzetti F, Reichenbach P, Wieczorek GF. 2003. Rockfall hazard and risk assessment in the Yosemite Valley, California, USA. *Natural Hazards and Earth Systems Science* **3**: 491–503.

Hantz D, Vengeon JM, Dussauge-Peisser C. 2003. An historical, geomechanical and probabilistic approach to rock-fall hazard assessment. *Natural Hazards and Earth Systems Science* **3**: 693–701.

Hergarten S. 2002. Landslides, sandpiles, and self-organized criticality. *Natural Hazards and Earth Systems Science* **3**: 505–514.

Hill BM. 1975. A simple general approach to inference about the tail of a distribution. *The Annals of Statistics* **3**: 1163–1174.

Hovius N, Stark CP, Allen PA. 1997. Sediment flux from a mountain belt derived by landslide mapping. *Geology* **25**: 231–234.

Hovius N, Stark CP, Hao-Tsu C, Jiun-Chuan L. 2000. Supply and removal of sediment in a landslide-dominated mountain belt: central range, Taiwan. *Journal of Geology* **108**: 73–89.

Hungr O, Evans SG, Hazzard J. 1999. Magnitude and frequency of rock falls along the main transportation corridors of southwestern British Columbia. *Canadian Geotechnical Journal* **36**: 224–238.

Hungr O, McDougall S, Wise M, Cullen M. 2008. Magnitude-frequency relationships of debris flows and debris avalanches in relation to slope relief. *Geomorphology* **96**(3–4): 355–365.

Hürlimann M, Rickenmann D, Graf C. 2003. Field and monitoring data of debris-flow events in the Swiss Alps. *Canadian Geotechnical Journal* **40**: 161–175.

Jaboyedoff M, Baillifard F, Bardou E, Girod F. 2004. The effect of weathering on Alpine rock instability. *Quarterly Journal of Engineering Geology & Hydrogeology* **37**: 95–103.

Katz O, Aharonov E. 2006. Landslides in vibrating sand box: what controls types of slope failure and frequency magnitude relations? *Earth and Planetary Science Letters* **247**: 280–294.

Koppes MN, Montgomery DR. 2009. The relative efficacy of fluvial and glacial erosion over modern to orogenic timescales. *Nature Geosciences* **2**: 644–647.

Korup O, Densmore AL, Schlunegger F. 2010. The role of landslides in mountain range evolution. *Geomorphology* **120**: 77–90.

Korup O, Görüm T, Hayakawa Y. 2012. Without power? Landslide inventories in the face of climate change. *Earth Surface Processes and Landforms* **37**: 92–99.

Lane SN, Westaway RM, Hicks DM. 2003. Estimation of erosion anddeposition volumes in a large, gravel-bed, braided river using synoptic remote sensing. *Earth Surface Processes and Landforms* **28**: 249–271.

Larsen IJ, Montgomery DR, Korup O. 2010. Landslide erosion controlled by hillslope material. *Nature Geosciences* **3**: 247–251.

Lavé J, Burbank D. 2004. Denudation processes and rates in the Transverse Ranges, southern California: Erosional response of a transitional landscape to external and anthropogenic forcing. *Journal of Geophysical Research* **109**: F01006. DOI: 10.1029/2003JF000023.

Li C, Ma T, Zhu X, Li W. 2011. The power-law relationship between landslide occurrence and rainfall level. *Geomorphology* **130**: 221–229.

Lim M, Rosser NJ, Allison RJ, Petley DN. 2010. Erosional processes in the hard rock coastal cliffs at Staithes, North Yorkshire. *Geomorphology* **114**: 12–21.

Malamud BD, Turcotte DL, Guzzetti F, Reichenbach P. 2004. Landslide inventories and their statistical properties. *Earth Surface Processes and Landforms* **29**: 687–711.

McArdell BW, Bartelt P, Kowalski J. 2007. Field observations of basal forces and fluid pore pressure in a debris flow. *Geophysical Research Letters* **34**: L07406. DOI: 10.1029/2006GL029183.

Moore JR, Sanders JW, Dietrich WE, Glaser SD. 2009. Influence of rock mass strength on the erosion rate of alpine cliffs. *Earth Surface Processes and Landforms* **34**: 1339–1352.

Pelletier JD, Malamud BD, Blodgett T, Turcotte DL. 1997. Scale-invariance of soil moisture variability and its implications for the frequency-size distribution of landslides. *Engineering Geology* **48**: 255–268.

Rickenmann D, Hürlimann M, Graf C, Näf D, Weber D. 2001. Murgang-Beobachtungsstationen in der Schweiz. *Wasser Energie Luft* **93**: 1–8.

Rousseau N. 1999. *Study of seismic signals associated with rockfalls at 2 sites on the Reunion island (Mahavel Cascade and Souffrière cavity)*. IPG: Paris.

Schlögel R, Torgoev I, De Marneffe C, Havenith HB. 2011. Evidence of a changing size-frequency distribution of landslides in the Kyrgyz Tien Shan. *Earth Surface Processes and Landforms* **36**: 1658–1669.

Schlunegger F, Badoux A, McArdell BW, Gwerder C, Schnydrig D, Rieke-Zapp D, Molnar P. 2009. Limits of sediment transfer in an alpine debris-flow catchment, Illgraben, Switzerland. *Quaternary Science Reviews* **28**: 1097–1105.

Schürch P. 2011. *Debris-flow Erosion and Deposition Dynamics*. Durham University: Durham, UK.

Schwab M, Rieke-Zapp D, Schneider H, Liniger M, Schlunegger F. 2008. Landsliding and sediment flux in the Central Swiss Alps: a photogrammetric study of the Schimbrig landslide, Entlebuch. *Geomorphology* **97**: 392–406.

Silverman BW. 1981. Using kernel density estimates to investigate multimodality. *Journal of the Royal Statistical Society. Series B (Methodological)* **43**: 97–99.

Simonett DS. 1967. Landslide distribution and earthquakes in the Bewani and Torricelli Mountains, New Guinea. In *Landform Studies from Australia and New Guinea*, Jennings JN, Mabbutt JA (eds). Cambridge University Press: Cambridge; 64–84.

Stark CP, Guzzetti F. 2009. Landslide rupture and the probability distribution of mobilized debris volumes. *Journal of Geophysical Research* **114**: F00A02. DOI: 10.1029/2008JF001008.

Stark CP, Hovius N. 2001. The characterization of landslide size distributions. *Geophysical Research Letters* **28**: 1091–1094.

Sugai T, Ohmori H, Hirano M. 1994. Rock control on magnitude–frequencydistribution of landslide. *Transactions of the Japanese Geomorphological Union* **15**: 233–351.

Taylor JR. 1997. *An Introduction to Error Analysis: the Study of Uncertainties in Physical Measurement*. University Science Books: Sausalito, CA.

Van Den Eeckhaut M, Poesen J, Govers G, Verstraeten G, Demoulin A. 2007. Characteristics of the size distribution of recent and historical landslides in a populated hilly region. *Earth and Planetary Science Letters* **256**(3–4): 588–603.

Zhang L. 2005. Automatic digital surface model (DSM) generation from linear array images. Report no 88, Institute of Geodesy and Photogrammetry, ETH Zurich, Switzerland.

Zhang L, Gruen A. 2006. Multi-image matching for DSM generation from IKONOS imagery. *ISPRS Journal of Photogrammetry and Remote Sensing* **60**: 195–211.

